Effect of 800 MeV proton irradiation on mechanical properties of BCC metals and alloys

by

Zihni Öztürk

A Thesis Submitted to the
Graduate Faculty in Partial Fulfillment of the
Requirements for the Degree of
MASTER OF SCIENCE

Major: Nuclear Engineering

Iowa State University
Ames, Iowa

1987

TABLE OF CONTENTS

LIST OF TABLES

LIST OF FIGURES

I. INTRODUCTION

Materials subjected to the irradiation environment have been studied to predict changes in their physical and mechanical properties. Irradiation of metals results in the production of the point defects and transmutation products. Subsequent diffusion of the irradiation produced defects generally leads to microstructural changes in a material with attendant mechanical and physical property changes.

Intense levels of radiation-produced defects in the form of atomic displacement cascades are produced in materials in fission and fusion reactor environments. Additional damage in the form of impurities, such as H, He, and heavier impurity atoms, is produced by higher energy neutrons or ions by means of nuclear reactions. Furthermore, the radiation produced defects and impurity atoms can interact with one another to produce special microstructural effects not seen in unirradiated materials. It is important to understand the effects of irradiation on the properties of fission and fusion reactor materials.

High energy proton accelerators may be used for radiation damage studies. Recently two high energy proton accelerators have become available: one at the Los Alamos Meson Physics Facility (LAMPF) at the Los Alamos National Laboratory in New Mexico, with a pulsating beam of 800 MeV protons, and one at the Swiss Institute for Nuclear Research

(SIN) at Villigen, Switzerland, with a steady beam of 600 MeV protons. The LAMPF accelerates the protons to 800 MeV at a design current of about 1 mA. The accelerator operates in a pulsed mode of a frequency of 120 Hz.

The LAMPF may be used for several different purposes. It can be used to carry out general radiation damage studies using the direct proton beam or the spallation neutrons produced at the beam stop. Another possible application of the LAMPF is to develop specific materials for its structures, such as beam line windows, beam line stops, and targets that are radiation damaged during irradiation. Especially, the beam line window is receiving considerable attention by investigators at SIN concerning modifications of the beam target at their 600 MeV proton accelerator and a collaborative research is underway at LAMPF.

Recently, an 1100 MeV proton accelerator with an average current of 5 mA was proposed by researchers at KFA-Jülich to serve as a spallation neutron source. To investigate materials for cladding and beam windows for this accelerator a joint Jülich-Los Alamos research program was set up [1].

The LAMPF and SIN protons have been used in radiation damage studies for various materials using the direct proton beam and spallation neutrons produced at the beam stop. In addition to producing atomic displacement damage in the

lattice, these protons generate H and He at very high rates through spallation reactions. The damage characteristics of high energy proton irradiations are very similar to those of fission and fusion neutrons, but the mechanisms of the energy transfer to the lattice atoms are rather different. The high energy protons produce spallation reactions in the target atoms. Spallation reactions occur in two stages: (1) intranuclear and internuclear cascade stage, and (2) deexcitation stage. In the first stage, the incident proton strikes one nucleon at a time within the nucleus, and the struck nucleons may strike other nucleons, which constitutes the intranuclear cascade. Some of the struck nucleons may escape from the nucleus and strike other nuclei where the process is repeated (internuclear cascade). In this fashion, a chain of internuclear interactions occurs until the ejected nucleon energy is reduced to an energy so low that no further interactions take place. At the end of the internuclear cascade, the product nucleus usually remains in an excited state. In the second stage of high energy reactions, the deexcitation of the nucleus takes place by evaporation of nucleons and light nuclei, or by fission. As a result of these spallation reactions, materials experience a special type of radiation damage and deposit a large amount of energy that result in atomic displacements and the production of H, He, and heavier transmutation products in

materials [2].

The purpose of this work is to analyze the effects of proton irradiations on the tensile properties of the BCC metals and alloys, Ta, Fe, Fe-2.25Cr-1Mo, and Fe-12Cr-1Mo (HT-9) using the engineering stress-strain charts which are the results of the 800 MeV proton irradiation experiments done by Brown et al. [3]. The Cr-Mo steels are considered as possible first-wall and blanket structure materials for fusion reactors operating up to about 520°C. The irradiation studies in fast breeder reactor research have indicated that 12Cr-1Mo steel could be used for this application because of its excellent swelling resistance [4]. Similar irradiation studies have been noted for the 2.25Cr-1Mo steel in the Breeder Reactor program [4]. It was also noted that the 12Cr-1Mo and 2.25Cr-1Mo steels are very suitable alloys for the proton beam window which is in contact with Pb-Bi, on the basis of the measured strength and ductility upon irradiation [3].

II. LITERATURE REVIEW

The 800 MeV LAMPF protons and 600 MeV SIN protons have been used for several material irradiation studies. Characterization of radiation damage induced by these high energy protons has been gaining considerable attention because of the possibility of extrapolating this information to high energy neutron damage produced in nuclear fission and especially fusion environments [5-8].

Coulter et al. calculated radiation damage effects of 800 MeV protons incident on a 1 cm thick Cu target [9]. In that study, radiation damage was found to be uniform across the sample and thus provided a reasonable simulation to radiation damage effects relevant to the fusion reactor applications. In the calculation of radiation damage effects of the 800 MeV protons in copper, The Nucleon-Meson Transport Code (NMTC) [10-13] was employed to calculate the nuclear interactions produced in the target material by the incident protons. The theory of Lindhard et al. [14-16] was employed in the determination of damage energy deposition in the target due to the energetic particle and nuclei evolved in the NMTC calculation.

One of the very important results of the calculations of Coulter et al. is that the damage energy cross section, σ_E, for the 800 MeV protons on copper is quite high, 350 barn-KeV, compared to 273 for 14 MeV neutrons, 83.2 for

U-235 neutrons, and 45.1 barn-KeV for the fission reactor neutrons at the Experimental Breeder Reactor (EBR-2). The corresponding displacement cross section is given by

$$\sigma_d = \frac{\beta \ \sigma_E}{2T_d} \tag{2.1}$$

which for β = 0.8 and the threshold displacement energy, T_d = 22 eV, gives σ_d = 6400 barns for the 800 MeV protons, 4963 for 14 MeV neutrons, 1512 for U-235 neutrons, and 820 barns for fission reactor neutrons at EBR-2 [9]. The ASTM standards give T_d = 30 eV for copper [17].

The higher displacement production rates for heavy ion bombardments and the corresponding contraction in the exposure time to achieve a given displacement concentration are largely responsible for the use of accelerators to simulate neutron radiation effects. However, there is an important drawback to the use of heavy ion bombardments, that is, the stopping power is very high (10^4 MeV/cm) [18]. On the contrary, for 800 MeV protons, the stopping power in Cr, Fe, Ni, and Cu is given as 12-15 MeV/cm [19]. For heavy-ion bombardments the defect generation rate as a function of penetration distance is extremely non-uniform, and great care must be exercised to take proper account of the spacial variation of the damage [2]. On the other hand, for 800 MeV proton bombardments, near uniformity of damage in centimeters thick samples is achieved, and quite high

damage energy and displacement cross sections are maintained [2].

One of the important considerations concerning radiation damage in fusion reactor structural materials is the embrittlement due to helium gas production. Conn gives the ratio of the He production (in appm/yr) to the displacement production (in dpa/yr) in 316 stainless steel as 15.4 for the fusion reactors, and 0.63 for the fission reactors, and similar results are given for other metals [20]. Coulter et al. indicate that the ratio of the He production to the displacement production in copper is 10 times greater for the 800 MeV protons and about 100 times smaller for the fission neutrons than the fusion neutrons [9]. In another radiation damage study, Sommer et al. calculated radiation damage effects of 800 MeV protons for Al, stainless steels, Mo, and W [21]. The displacement cross sections for the four materials are 1400, 4100, 7700, and 14000 barns, respectively, to be compared to 6400 barns for copper. Altogether, the displacement cross sections are quite high for the 800 MeV protons.

Sommer et al. studied radiation-produced defects in Al by using transmission electron microscopy [22]. In that experiment, Al specimens were irradiated at 50°C with the LAMPF 800 MeV protons. Some of the specimens were cyclically stressed during irradiation. Cyclic stressing

during irradiation reduced both the number of voids and the size of voids formed in the aluminum. This was consistent with a model of Weertman and Green which predicts that moving dislocations should be better vacancy sinks than stationary ones [23]. In addition, Sommer et al. made a kinetic analysis to determine the effects of arbitrary numbers of repeated pulses and their associated radiation produced temperature oscillations on the material structure [24]. It was found that pulsing irradiation has no direct effect on material swelling and void growth.

In another experiment, Farnum et al. observed radiation-produced defects in W and Mo by using field ion microscopy [25]. In that experiment, 0.075 mm tungsten and molybdenum wires were irradiated with the 800 MeV protons at an ion current of 5-8 μA for 10 days at ambient temperature. Following irradiation, field-ion microscopy analyses were made at 78°K utilizing an exchange medium of 90% helium and 10% neon. Tungsten samples showed a few vacant lattice sites as well as a defect zone, while Mo samples exhibited excessive numbers of vacancies and vacancy clusters.

Systematic experimental studies of temperature, stress, total fluence, and helium effects have been conducted on aluminum [26-30]. Green et al. studied the effects of high helium production rate on microstructural evolution in aluminum during 600 MeV proton irradiation. Samples of

high-purity aluminum were irradiated at 120°C with 600 MeV protons to 0.2, 0.6, and 2 dpa [26]. Transmission electron microscopy on specimens irradiated to 0.2 and 0.6 dpa showed the presence of cavity-denuded zones (CDZ) along grain boundaries and cavity-containing zones (CCZ) adjacent to the CDZ. At the dose level of 2 dpa, a dense population of very small cavities is resolved on or near grain boundaries.

Jang et al. investigated formation of irradiation-induced defects in proton irradiated high-purity aluminum using transmission electron microscopy [30]. The specimens were irradiated by 800 MeV protons to about 0.25 dpa, producing about 20 appm He, 130 appm H, and approximately 70 appm of spallation products. The irradiated specimens were found to contain a high concentration of cavities, joggy dislocations, black spots, and dislocation loops. A post irradiation annealing treatment at 250°C resulted in complete disappearance of small cavities and formation of gas bubbles on grain boundaries.

In another study, Green calculated radiation damage effects of 600 MeV protons incident on a 10 mm thick aluminum target [31]. This calculation was repeated for 800 MeV protons for comparison. The calculated damage characteristics produced by 600 MeV proton irradiation of aluminum, copper, type 316 stainless steel, titanium, vanadium, and molybdenum were also reported [31].

Brown and Cost measured radiation hardening and embrittlement by tensile tests on 800 MeV proton irradiated 304 SS, Alloy 718 (18.5Fe-19Cr-52.5Ni-3Mo), Ta, and Mo [32]. In that experiment, tensile samples were directly water cooled during irradiation and were tested at room temperature. For the 304 SS and annealed Alloy 718, the yield strengths increased by about a factor of 3 and 1.6, respectively, while the ductility decreased by about 30% and 40%. In the BCC metals (Ta and Mo), the yield strengths increased by at least a factor of 2. Tantalum samples retained significant ductility at room temperature, while several molybdenum specimens broke at less than 0.2% strain.

The newly developed metallic glasses have some special properties that make them very attractive for some technological applications. These amorphous metallic glasses could be useful as structural materials for fusion and fission reactors. Cost and Sommer made resistivity measurements on a number of samples to investigate the response of metallic glasses to irradiation [33].

As mentioned before, investigaters at SIN have been working on a research program to develop materials for their 600 MeV proton accelerator beam line windows. Materials that will be chosen for this service must be compatible with the molten Pb-Bi and retain reasonable ductility and strength during 600 MeV proton irradiation to fluences of

10^{25} p/m^2 at a temperature 673°K. Collaborative work is underway at LAMPF to test materials for SIN windows. Initial studies and examinations have indicated that BCC metals and alloys, Fe, Ta, Fe-2.25Cr-1Mo, and Fe-12Cr-1Mo (HT-9), could be candidates for this application.

Recently, Brown et al. examined the mechanical property changes in these BCC metals and alloys to find out whether they could be useful as structural materials for proton accelerator beam line windows in contact with Pb-Bi [3]. In that experiment, sheet tensile samples, 0.5-mm thick, of the four materials were fabricated and heat treated as described in Table 1, which also gives some comments on the resulting microstructures [3].

TABLE 1. Sample heat treatments [3]

Material	Temperature (K)	Time (min)	Comments
Ta	1523	60	Not recrystallized
Fe	1193	5	About 0.5-mm diameter grains
Fe-2.25Cr-1Mo	1213	7	10-20 mm grain size
	873	30	Not fully hardened
Fe-12Cr-1Mo	1323	7	Martensitic
	973	60	

The samples were sealed inside capsules containing Pb-Bi and were proton-irradiated at LAMPF to two fluences, 4.8 x 10^{23} p/m^2 for the low-fluence samples and 5.4 x 10^{24}p/m^2 for the high-fluence samples. The beam current was approximately equal to the 1 mA anticipated for the upgraded SIN accelerator. The power deposited by the proton beam in the capsules was sufficient to maintain sample temperatures of about 673°K. Post-irradiation tensile tests were conducted at room temperature at a strain rate of 9 x 10^{-4} s^{-1}. A clip-on extensometer was used to monitor strain during the first portion of the test. At about 5 percent strain, it was necessary to remove the extensometer, and the test was continued with crosshead displacement as the measure of strain.

In this study, the effects of 800 MeV proton irradiations on the tensile properties of these BCC metals and alloys were analyzed in terms of Young's modulus and strain hardening parameters using the engineering stress-strain charts obtained in [3].

III. STRESS-STRAIN DIAGRAMS

The application of mechanical forces to a solid body causes the body to change shape (deform) and, in some cases, to break (fracture). These responses define the mechanical properties that were analyzed in this work. Of special importance are stress and strain, which will be defined later. These quantities were used to characterize the behavior of materials.

The load (lbs)-distance (inch) charts for four material samples were obtained from the experiments described in [3]. A typical chart is shown in Figure 1.

As mentioned before, a clip-on extensometer was used to monitor the strain during the first portion (part A in Figure 1) of the test. At point C (Figure 1), it was necessary to remove the extensometer, and the rest of the test was continued with the crosshead displacement as the measure of the strain. To be able to analyze the effect of 800 MeV proton irradiations on the mechanical properties of the materials, these load-distance charts were first converted to the engineering stress (ksi)-strain (%) diagrams and then to true stress-strain diagrams. The conversion from chart inches to strain was done for the first part (A) and second part (B) separately.

During the first portion (part A) of the test, the chart was driven by the output of the extensometer, so that

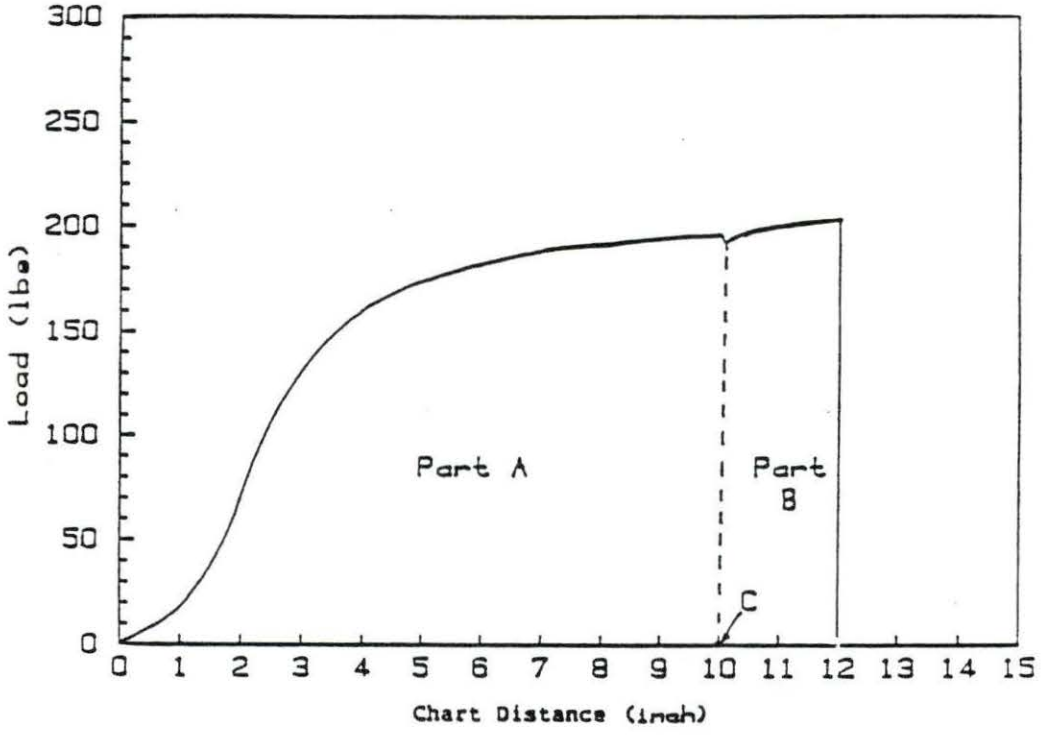

FIGURE 1. A load-distance chart, as obtained from the tensile test

one chart inch corresponded to a 0.1% relative increase in the distance between the arms of the extensometer. Since the gage length of the extensometer was 2 inches, one inch on the chart corresponded to an extension of 0.001x2=0.002 inches. Since the gage length of the sample was 0.375 inch (Figure 2), the strain in the sample corresponding to point C in Figure 1 or 10 chart inches is

$$\epsilon_A = \frac{\Delta L}{L_0} = \frac{0.02}{0.375} = 0.0533 = 5.33\% \qquad (3.1)$$

The early region of part A in Figure 1 shows a concave upward shape, which is due to the taking up of slack in the load system at points inside the extensometer arms, but outside the gage section of the sample. Thus, in this region, the extensometer output is driving the chart but the sample is not straining and the load is increasing only slightly. This is an unavoidable problem associated with the need to employ sub-size samples.

The extensometer was so arranged that it was necessary to remove it after an extension of 0.02 inches (10 chart inches). Therefore, during the second part (part B, Figure 1) of the test, the crosshead motion distance was used as a measure of the strain. The crosshead speed was 0.02 inch/min and the chart speed was 2 inch/min. Therefore, one inch on the chart corresponds to 0.01 inch extension. Thus, the strain for part B is

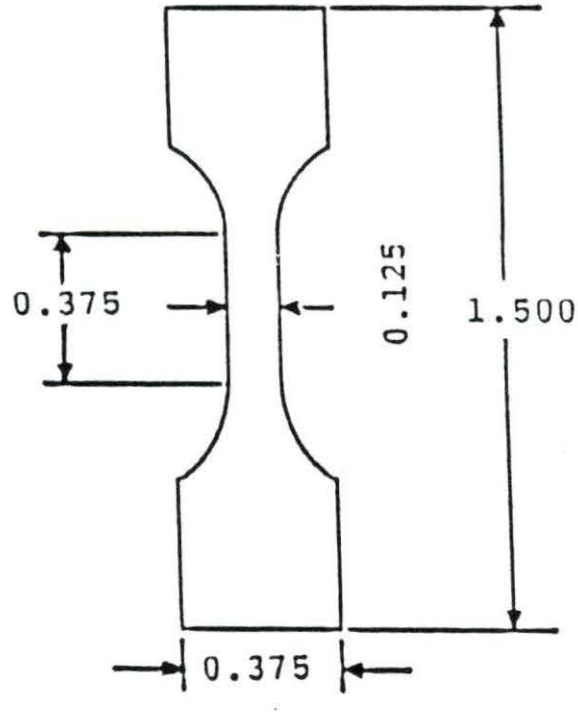

FIGURE 2. Sheet tensile sample, thickness, 0.127 inches

$$\epsilon_B = \frac{0.01\ d}{L_0} = \frac{0.01\ d}{0.375} = 0.0266\ d \qquad (3.2)$$

or

$$\epsilon_B(\%) = 2.66\ d \qquad (3.3)$$

where d is the distance in inches from point C in Figure 1 to the point where the strain is being determined. Hence, the total strain for part A and part B together is

$$\epsilon = \epsilon_A + \epsilon_B \qquad (3.4)$$

or

$$\epsilon(\%) = 5.333 + 2.666\ d \qquad (3.5)$$

The engineering stress is defined as the force per unit original cross-sectional area acting on a material and given by

$$\sigma = \frac{P}{A_0} \qquad (3.6)$$

where σ is the engineering stress, P is applied load (lbs), and A_0 is the initial cross-sectional area of the sample (in^2), which gives stress in psi.

The conversions for the engineering strain and stress were carried out by using the relations discussed above, i.e, for strain less than 5.33%, equation (3.1); for strain greater than 5.33%, equation (3.5); and for stress, equation (3.6). The original cross-sectional areas (A_0) and the full-scale loads are given in Tables 2-5 for the samples of

the four types of materials.

TABLE 2. Area (A_0) and full-scale load for Ta samples

Sample	Area (A_0) (in^2)	Full-Scale Load (lbs)
Unirradiated		
Ta-13	0.00197	120
Ta-14	0.00197	120
Ta-15	0.00197	120
Ta-16	0.00195	120
Low irradiated		
Ta-1	0.00197	120
Ta-2	0.00195	120
Ta-11	0.00194	120
Ta-12	0.00188	120
High irradiated		
Ta-3	0.00193	300
Ta-4	0.00185	300
Ta-5	0.00193	300
Ta-6	0.00192	300

The load-distance charts were digitized to obtain the engineering stress-strain diagrams and data files for later analyses. Since the charts were very large in size for the digitizer, they were digitized in two parts separately and then appended to each other. The digitizing process was done by using the Hipad computer program written in Uniaps Comal language and the following Commodore computer apparatus:

1. Disk drive : Commodore-1541

TABLE 3. Area (A_0) and full-scale load for Fe samples

Sample	Area (A_0) (in^2)	Full-Scale Load (lbs)
Unirradiated		
Fe-8	0.00258	60
Fe-9	0.00264	60
Fe-10	0.00276	60
Fe-18	0.00253	60
Fe-19	0.00274	60
Fe-20	0.00257	60
Low irradiated		
Fe-1	0.00243	60
Fe-2	0.00150	120
Fe-16	0.00179	60
High irradiated		
Fe-3	0.00206	120
Fe-4	0.00202	120
Fe-5	0.00202	120

2. Digitizer : Hipad TM digitizer

3. Computer : Commodore-64

4. Video monitor : Commodore, model 1702

5. Printer : Okidata-120

6. Plotter : Hewlett-Packard, model 7225A

In plotting a stress-strain curve, there are two different systems of stress-strain that can be used. One system, the engineering stress-strain, is based on the initial dimensions of the test samples, while the second system, the true stress-strain, is based on the instantaneous sample dimensions. The engineering system is

TABLE 4. Area (A_0) and full-scale load for Fe-2.25Cr-1Mo samples

Sample	Area (A_0) (in^2)	Full-Scale Load (lbs)
Unirradiated		
C-14	0.00250	600
C-15	0.00250	300
C-16	0.00254	300
C-17	0.00253	300
C-18	0.00185	300
C-21	0.00133	300
C-23	0.00254	300
C-24	0.00251	300
Low irradiated		
C-2	0.00184	300
C-3	0.00208	300
C-12	0.00178	300
C-13	0.00186	300
High irradiated		
C-6	0.00177	300
C-7	0.00168	300

used for convenience, but does not give an accurate description of the actual behavior of the materials at strains above about 10%. Thus, at higher strains it sometimes becomes necessary to use true stress and strain. True stress takes into account the fact that the load-bearing area decreases with increasing strain. In the elastic region (strain generally lower than about 0.5%), the engineering stress and the true stress are essentially the same, and similarly for engineering strain and true strain.

TABLE 5. Area (A_0) and full-scale load for Fe-12Cr-1Mo (HT-9) samples

Sample	Area (A_0) (in^2)	Full-Scale Load (lbs)
Unirradiated		
HT-11	0.00271	600
HT-12	0.00275	600
Low irradiated		
HT-1	0.00244	600
HT-2	0.00270	600
HT-9	0.00260	600
HT-10	0.00262	600
High irradiated		
HT-4	0.00272	600
HT-5	0.00272	600

The following quantities can be defined to further describe the two stress-strain systems:

L_0 = initial gage length of undeformed specimen

L = instantaneous gage length after some deformation has occurred

A_0 = initial cross-sectional area

A = instantaneous cross-sectional area after some deformation has occurred

P = applied load

The true stress is defined as

$$\bar{\sigma} = \frac{P}{A} \tag{3.7}$$

The engineering strain is defined as

$$\epsilon = \frac{L-L_0}{L_0} \tag{3.8}$$

whereas the true strain is defined as

$$\bar{\epsilon} = \mathrm{Ln}(L/L_0) = \mathrm{Ln}(1+\epsilon) \tag{3.9}$$

If there is no volume change in the specimen during the deformation, the following relation is valid between the true stress and the engineering stress

$$\bar{\sigma} = \sigma(1+\epsilon) \tag{3.10}$$

Since we may be working in the region where the strain is larger than 10%, it is necessary to convert the engineering stress-strain diagrams to true stress-strain diagrams to be able to analyze the work hardening.

As mentioned above, the observed shapes of the load-distance chart curves are not a true reflection of the actual behavior of the materials in the low strain region, due to the taking up of slack in the load chain at regions inside the extensometer arms but outside of the sample gage length. This is shown in Figure 3 in terms of engineering stress versus apparent engineering strain. Because the strain is only apparent, the attempt was made to obtain a more valid indication of the material behavior in the low strain region. This was done by performing the following steps:

1. Determine the inflection point on the stress-strain curve (σ-ϵ). To determine the inflection point (point of maximum slope), a least-squares straight line was evaluated for each group of five adjacent digitized points. This yielded an approximate point of maximum slope, S_{max}, and it permitted the evaluation of the approximate strains ϵ_1 and ϵ_2 corresponding to $S_{max}/2$, as shown in Figure 3. For Fe-10, C-14, and C-18 samples, there were not enough data points between S_{max} and $S_{max}/2$. Therefore, it was necessary to take some additional data points whose corresponding slopes were smaller than $S_{max}/2$. Then, a least-squares polynomial fit was made to the digitized points between ϵ_1 and ϵ_2. A third-degree polynomial regression was used, with σ given by

$$\sigma = A_0 + A_1\epsilon + A_2\epsilon^2 + A_3\epsilon^3 \qquad (3.11)$$

and the best-fit values of A_0, A_1, A_2, A_3 were obtained. Figure 4 shows the polynomial-fitted curve in the region $\epsilon_1 < \epsilon < \epsilon_2$.

2. The maximum slope was determined as follows: From Equation 3.11

$$S = \text{slope} = \frac{d\sigma}{d\epsilon} = A_1 + 2A_2\epsilon + 3A_3\epsilon^2 \qquad (3.12)$$

If we take the derivative of Equation 3.12, then

$$\frac{dS}{d\epsilon} = \frac{d^2\sigma}{d\epsilon^2} = 2A_2 + 6A_3\epsilon \qquad (3.13)$$

The maximum slope corresponds to

$$\frac{dS}{d\epsilon} = 0 \tag{3.14}$$

whereby, the strain at the inflection point is

$$\epsilon_i = -\frac{A_2}{3A_3} \tag{3.15}$$

and the maximum slope, by Equation 3.12, is

$$S_{max} = A_1 + 2A_2\epsilon_i + 3A_3\epsilon_i^2$$

$$= A_1 - \frac{A_2^2}{3A_3} \tag{3.16}$$

3. The slope of stress-strain curve in the elastic region was tentatively assumed to correspond to S_{max}, i.e, assumed to correspond to the slope of the modulus line or to Young's modulus. Thus, for strains below the inflection point at $\epsilon = \epsilon_i$, the stress-strain curve was linearly extrapolated with slope S_{max}, as indicated by the line PQ in Figure 5. The strain at point P where $\sigma = 0$ is labelled ϵ_0, which is given by

$$\epsilon_0 = \epsilon_i - \frac{\sigma_i}{S_{max}} \tag{3.17}$$

where σ_i is the stress at the inflection point. ϵ_0 was calculated by using Equation 3.17.

4. The stress-strain curve was then translated to lower strains, so as to bring $\sigma = 0$ at $\epsilon = 0$. The translated curve

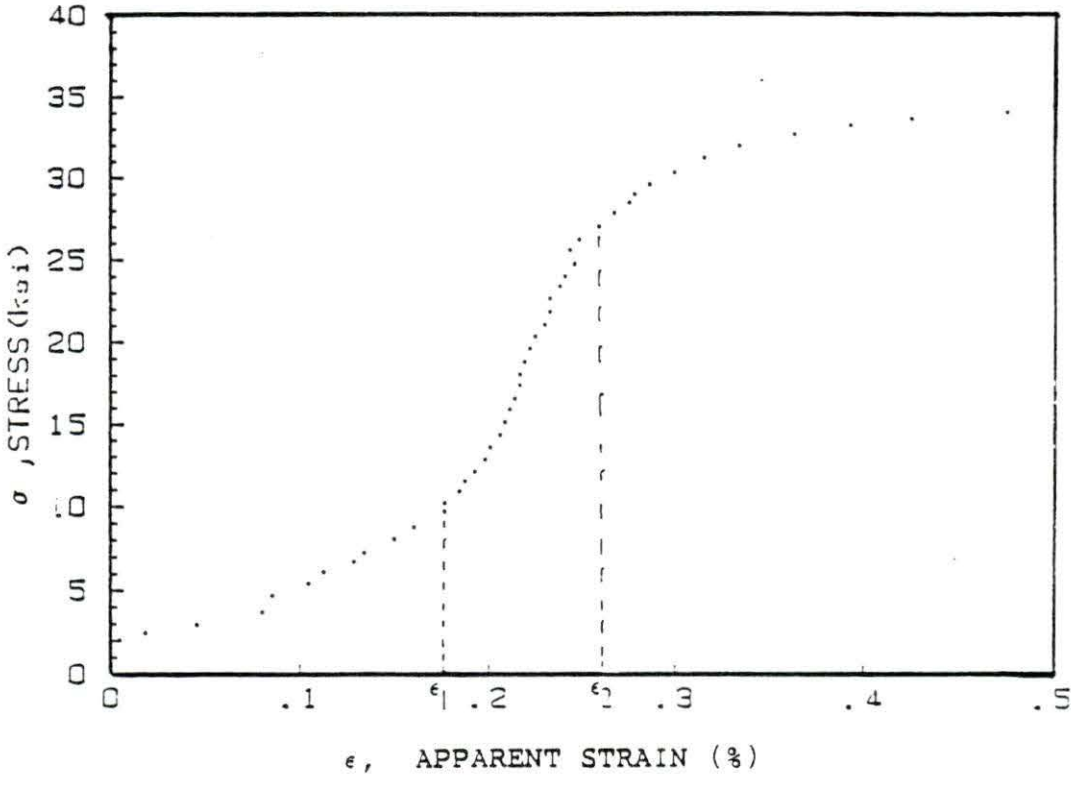

FIGURE 3. Digitized points for engineering stress versus apparent engineering strain curve for a high-irradiated sample (Fe-4)

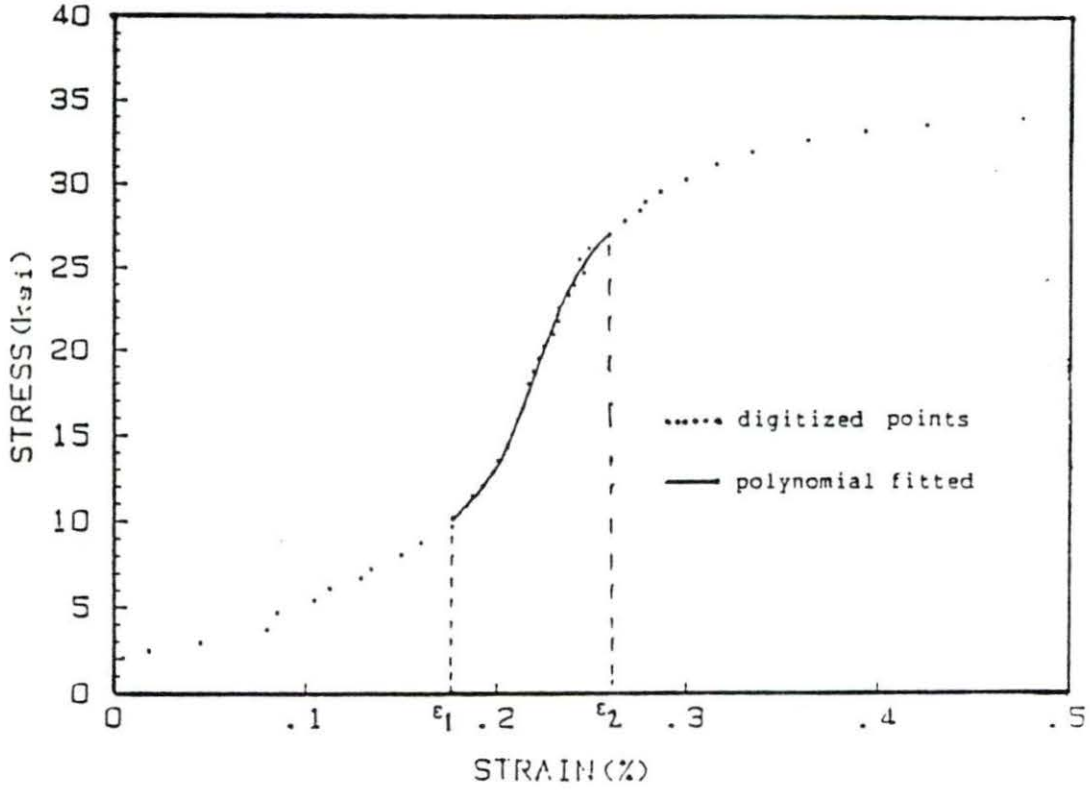

FIGURE 4. A digitized engineering stress-strain curve and a polynomial-fitted stress-strain curve for a high-irradiated Fe-4 sample, in the region $\epsilon_1 < \epsilon < \epsilon_2$

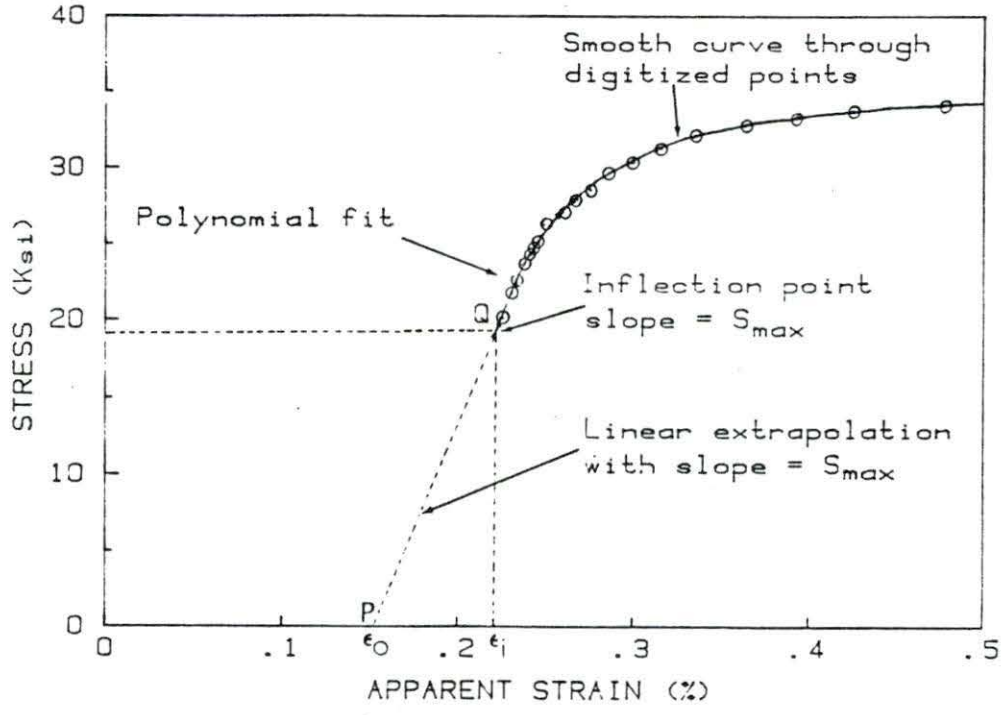

FIGURE 5. Engineering stress-strain curve for the high-irradiated Fe-4 sample, showing three regions: (1) linear extrapolated region, (2) polynomial fitted region and (3) smooth curve through digitized points

for the high-irradiated Fe-4 sample is shown in Figure 6.

5. The engineering stress-strain (σ-ϵ) curves were then converted to true stress-strain ($\bar{\sigma}$-$\bar{\epsilon}$) curves, using the relations between these two systems

$$\bar{\sigma} = \sigma(1+\epsilon) \tag{3.18}$$

and

$$\bar{\epsilon} = \mathrm{Ln}(1+\epsilon) \tag{3.19}$$

Figure 7 shows the engineering stress-strain (σ-ϵ) and true stress-strain ($\bar{\sigma}$-$\bar{\epsilon}$) curves for the unirradiated Fe-2.25Cr-1Mo sample C-15.

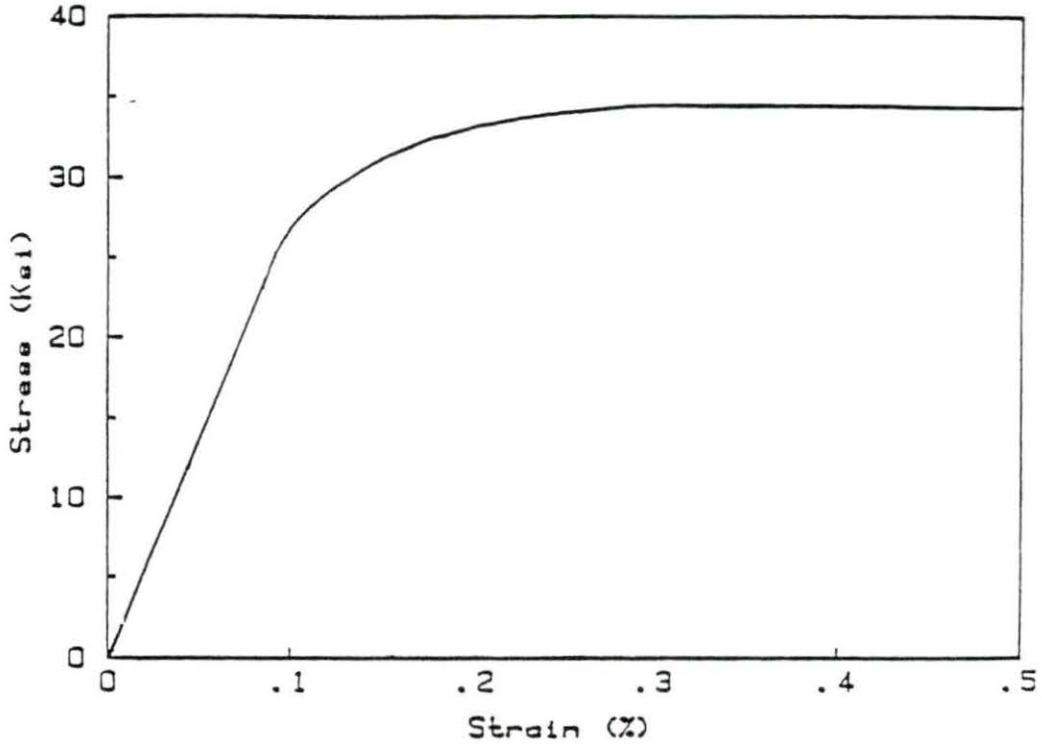

FIGURE 6. The translated engineering stress-strain curve for the high-irradiated Fe-4 sample

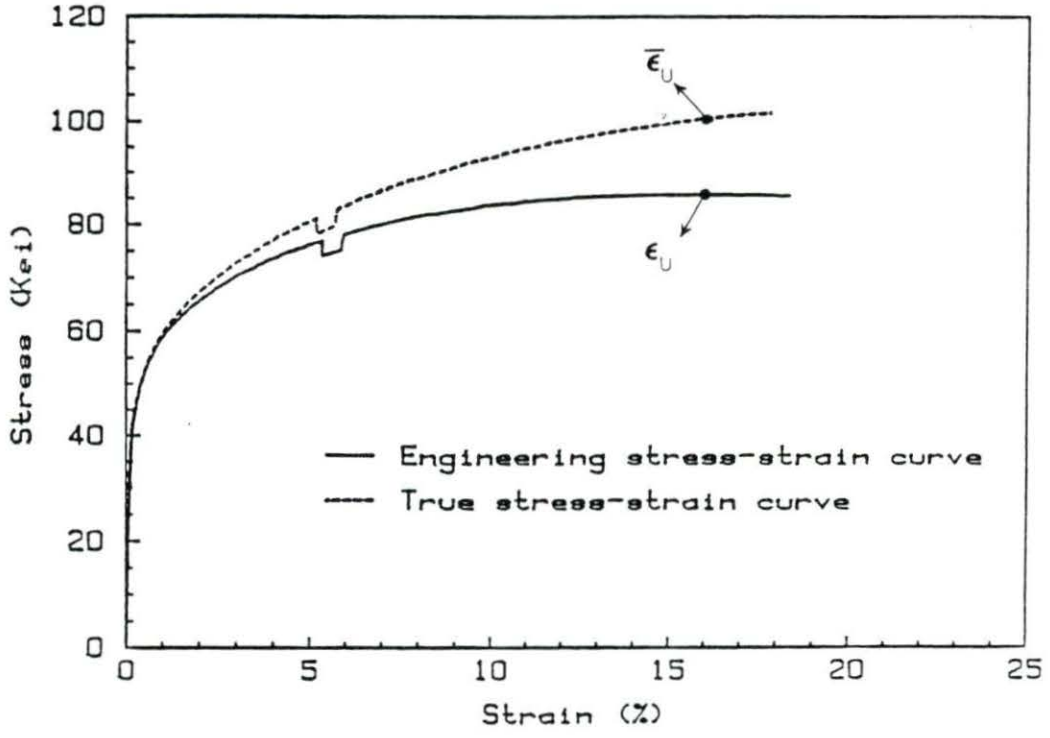

FIGURE 7. Engineering stress-strain (σ-ϵ) and true stress-strain (σ-ϵ) curves for unirradiated Fe-2.25Cr-1Mo sample C-15

IV. YOUNG'S MODULUS AND WORK HARDENING

In this chapter, the Young's modulus and the work hardening parameters are discussed. These are two important mechanical properties of materials in studying the effects of high energy proton irradiation.

IV.1. Young's Modulus

When solid materials are subjected to low stresses, they usually respond in an elastic fashion; that is, the strain produced by the stress is reversible, which means that the strain returns to zero when the stress is removed. Also, the strain is proportional to stress in this region, as expressed by Hooke's law. For a uniaxial applied tensile stress, σ, Hooke's law is simply

$$\sigma = E\epsilon \tag{4.1}$$

where the constant of proportionality, E, is known as the Young's modulus. This relationship is normally valid only for low strains (below about 0.5%).

Young's modulus is only slightly influenced by small variations in internal structure, such as small additions of alloying elements or the presence of defects like vacancies, dislocations, or grain boundaries. For alloys that show complete solid solubility, the Young's modulus usually varies linearly with composition. Alloys that form

intermediate phases have a much more complex composition dependence of the Young's modulus. The general rule is then; the stronger the interatomic forces, the higher the modulus [34].

In addition to the composition dependence of the Young's modulus, there is also a crystallographic variation in modulus; that is, if we measure E along different crystallographic directions in a single crystal, we get different values. This directional variation is known as anisotropy. The samples considered in this study were polycrystalline, for which the effect of crystalline anisotropy was averaged out. Finally, Young's modulus decreases with increasing temperature. Generally, the decrease is approximately linear with temperature up to about half the melting point (in°K), and the modulus decreases more rapidly with further increase in temperature [34].

As discussed in Chapter III, an attempt was made to associate the maximum slope, S_{max}, of the stress-strain curve in the low strain region with Young's modulus. Values of S_{max} for all of the samples tested are given in Tables 6-9. The average S_{max} for the unirradiated materials are compared with literature values of Young's modulus in Table 10. It is seen that the average S_{max} values are much lower than the expected values of Young's modulus.

TABLE 6. S_{max} for Ta samples

Sample	S_{max} 10^6(psi)
Unirradiated	
Ta-13	11.78
Ta-14	10.62
Ta-15	9.92
Ta-16	9.32
Low irradiated	
Ta-1	4.31
Ta-2	9.29
Ta-11	5.33
Ta-12	7.62
High irradiated	
Ta-3	2.83
Ta-4	3.72
Ta-5	4.58
Ta-6	5.86

IV.2. Work Hardening

At higher stress levels the slope of the stress-strain curve becomes much lower and Hooke's law no longer describes the relation between stress and strain. This region is known as the plastic region and is characterized by the fact that the deformation becomes permanent, or plastic. When the stress is removed, the material unloads elastically, but a permanent strain remains in material.

The applied tensile stress required to induce plastic behavior is known as the elastic limit or yield stress.

TABLE 7. S_{max} for Fe samples

Sample	S_{max} 10^6(psi)
Unirradiated	
Fe-8	4.31
Fe-9	6.58
Fe-10	8.20
Fe-18	4.29
Fe-19	4.65
Fe-20	2.44
Low irradiated	
Fe-1	4.99
Fe-2	1.79
Fe-16	3.86
High irradiated	
Fe-3	2.79
Fe-4	30.1
Fe-5	3.03

This stress is rather important in structural design, because it marks the limit at which small deformations are produced by small increases in stress. The increase in stress required to continue the plastic deformation at a given strain rate in the plastic region is called work hardening or strain hardening. The more a material is plastically deformed, the more difficult it becomes to plastically deform the material further.

As plastic deformation continues, the cross-sectional area decreases, but the load-carrying capacity of the specimen increases due to the work hardening. The maximum

TABLE 8. S_{max} for Fe-2.25Cr-1Mo samples

Sample	S_{max} 10^6(psi)
Unirradiated	
C-14	56.10
C-15	28.90
C-16	15.70
C-17	11.81
C-18	58.88
C-21	8.05
C-23	5.32
C-24	4.30
Low irradiated	
C-2	4.93
C-3	6.08
C-12	4.58
C-13	9.24
High irradiated	
C-6	5.88
C-7	6.45

load that the specimen can withstand defines a common engineering property, the ultimate tensile strength. In the plastic region the stress-strain curves for many materials are observed to obey the following relation [34,35]:

$$\bar{\sigma} = K\bar{\epsilon}^n \tag{4.2}$$

where K is a strength constant and n is a work hardening exponent. If we take the logarithm of equation (4.2), then

$$\ln(\bar{\sigma}) = \ln(K) + n\ln(\bar{\epsilon}) \tag{4.3}$$

which is a straight line equation and can be expressed as

TABLE 9. S_{max} for Fe-12Cr-1Mo (HT-9) samples

Sample	S_{max} 10^6(psi)
Unirradiated	
HT-11	7.59
HT-12	7.26
Low irradiated	
HT-2	2.33
HT-9	4.99
HT-10	2.13
High irradiated	
HT-4	3.80
HT-5	5.51

TABLE 10. Comparison between average S_{max} for unirradiated samples and literature values of Young's modulus

Material	Average S_{max} 10^6(psi)	Young's modulus 10^6(psi)	Reference number
Ta	10.4 ± 0.813	27	34
Fe	5.1 ± 1.461	29	34
Fe-2.25Cr-1Mo	23.7 ± 18.24	30	39
Fe-12Cr-1Mo	7.4 ± 0.165	27	39

$$y = a + bx \tag{4.4}$$

where $y = \ln(\bar{\sigma})$, $a = \ln(K)$, and $bx = n\ln(\bar{\epsilon})$.

For the four materials, the engineering stress-strain data were converted to true stress-strain data, and then these data were fitted to equation (4.3) to obtain the constants lnK and n. Some of the observed curves (C-14, C-15, HT-11, and HT-12) of ln(true stress)-ln(true strain) were very close to a straight line and some of them (Ta-13, Ta-14, Fe-8, and Fe-9) were upward concave in shape (Figure 8), so that the values of K and n were found by using a linear least-squares fit to the Ln-Ln data between 0.2% offset yield stress and ultimate tensile strength. The values of K, n, and true uniform strain are given in Tables 11-14 for the samples of four materials. The discontinuity between A and B in Figure 8 is due to the removal of the extensometer at about 5% strain. As mentioned before, after the removal of the extensometer, the rest of the test was continued with the crosshead motion as a measure of the strain.

R^2 values were calculated to check the goodness of fit to the actual data distribution. R^2 is known as the coefficient of determination and interpreted as the proportionate reduction of total variation in y associated with the use of independent variable x and given by [36]

$$R^2 = \frac{SSTO-SSE}{SSTO} \qquad (4.5)$$

where SSTO is the sum of the squared deviations from the

mean given by $\Sigma(y_i-\overline{y})^2$ and SSE is the error sum of squares given by $\Sigma(y_i-y(x_i))^2$, and in these expressions, y_i is the observed value, $y(x_i)$ is the predicted value, and $\overline{y}$ is the mean of the observed values of y. If all the observations fall on the fitted regression line, SSE = 0, and therefore, $R^2 = 1$. Thus, the larger is R^2, the more is the total variation of y reduced by introducing independent variable x. In other words, the larger is R^2, the better is the fit to the observed data. For all the samples tested, the value of R^2 was found to be between 0.95 and 0.99. Hence, it can be said that the work hardening equation (4.2) describes quite well the observed shape of the stress-strain curve in the work hardening region.

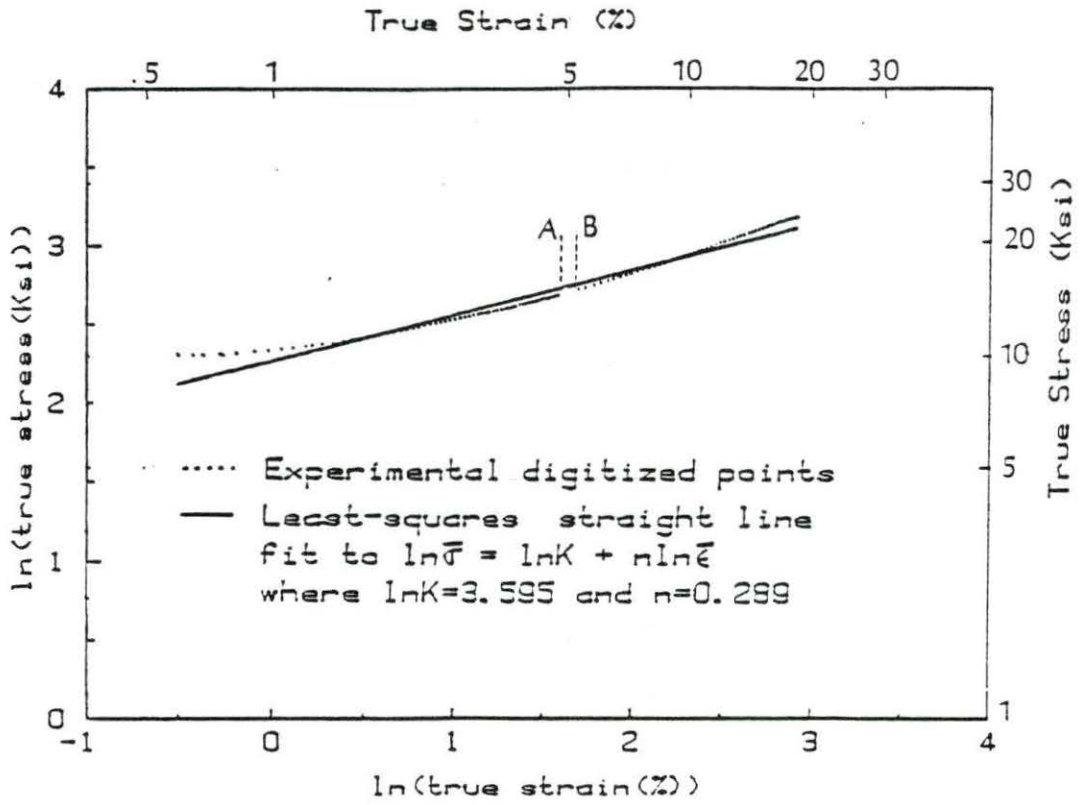

FIGURE 8. Ln(true stress)-Ln(true strain) curves for an unirradiated Fe-8 sample

TABLE 11. Work hardening parameters for Ta

Sample	Strength coefficient K (Ksi)	Work hardening exponent,n	True uniform strain
Unirradiated			
Ta-13	80.07	0.126	0.152
Ta-14	82.27	0.151	0.161
Ta-15	83.76	0.127	0.128
Ta-16	78.81	0.131	0.145

TABLE 12. Work hardening parameters for Fe

Sample	Strength coefficient K (Ksi)	Work hardening exponent,n	True uniform strain
Unirradiated			
Fe-8	36.42	0.288	0.195
Fe-9	32.00	0.192	0.191
Fe-10	41.16	0.298	0.257
Fe-18	46.84	0.286	0.283
Fe-19	43.72	0.311	0.307
Fe-20	41.13	0.342	0.277

TABLE 13. Work hardening parameters for Fe-2.25Cr-1Mo

Sample	Strength coefficient K (Ksi)	Work hardening exponent,n	True uniform strain
Unirradiated			
C-14	135.74	0.180	0.136
C-15	144.88	0.195	0.160
C-16	151.73	0.200	0.170
C-17	136.91	0.179	0.160
C-18	147.92	0.214	0.170
C-21	134.34	0.231	0.136
C-23	159.14	0.243	0.175
C-24	162.80	0.262	0.171
High fluence			
C-6	159.72	0.129	0.127
C-7	132.70	0.107	0.116

TABLE 14. Work hardening parameters for Fe-12Cr-1Mo (HT-9)

Sample	Strength coefficient K (Ksi)	Work hardening exponent,n	True uniform strain
Unirradiated			
HT-11	214.22	0.173	0.087
HT-12	220.53	0.176	0.095
High fluence			
Ht-4	232.76	0.230	0.126
HT-5	239.73	0.193	0.105

V. RESULTS AND DISCUSSION

Tables 6-9 show the values of the maximum slope, S_{max}, in the early regions of the stress-strain curve for all of the samples tested. It can be seen that there is considerable scatter in the values obtained, which indicates that the tensile tests were too crude to enable a reasonably accurate value of Young's modulus to be determined. This is perhaps only to be expected, since the apparatus used for both unirradiated and irradiated samples was designed to be operated remotely in the hot cells. In the very low strain region where the deformation is elastic (below about 0.5%), it is difficult to avoid some spurious extension due to the apparatus itself rather than the straining of the sample. This would cause the strain to appear to be higher than it actually is in the sample, and thus would yield an abnormally low slope to the stress-strain curve in the elastic region. As a result, the observed values of S_{max} would be lower than true Young's modulus. Furthermore, this would be expected to be especially the case for the irradiated samples, for which the alignment of the samples in the tensile machine was particularly difficult, and the observed S_{max} values are indeed lower in Tables 6-9 for irradiated case. At any rate, it can be concluded that the values of S_{max} do not correspond accurately to Young's modulus, as can be seen in Table 10 for the unirradiated

materials, where some comparison with literature values of Young's modulus is possible.

Figures 9-12 show the digitized engineering stress-strain curves for all of the samples tested. For irradiated Ta and Fe, Figures 9 and 10, respectively, show the onset of plastic instability immediately upon plastic deformation. Thus, the yield and ultimate tensile stresses were coincident, and no work hardening was exhibited. Therefore, the stress-strain curves for irradiated Ta and Fe were not analyzed in terms of work hardening. That is why the values of K and n for high irradiated samples of the Ta and Fe are not included in Tables 11-14. Also, the values of K and n are not given in Tables 11-14 for low irradiated samples of four materials. One reason for this is that some low irradiated samples, especially samples of the Fe and Ta showed very little work hardening, so that there was not enough data to fit to the work hardening equation (4.2). Another reason is that anomalous shapes were obtained for the stress-strain curves of many low irradiated samples of the four materials; this made the evaluation of the work hardening parameters not reasonable.

The value of the work hardening exponent, n, should be numerically equal to the true uniform strain if the true stress-strain curve fits the work hardening equation. A comparison of the values of n and true uniform strain in

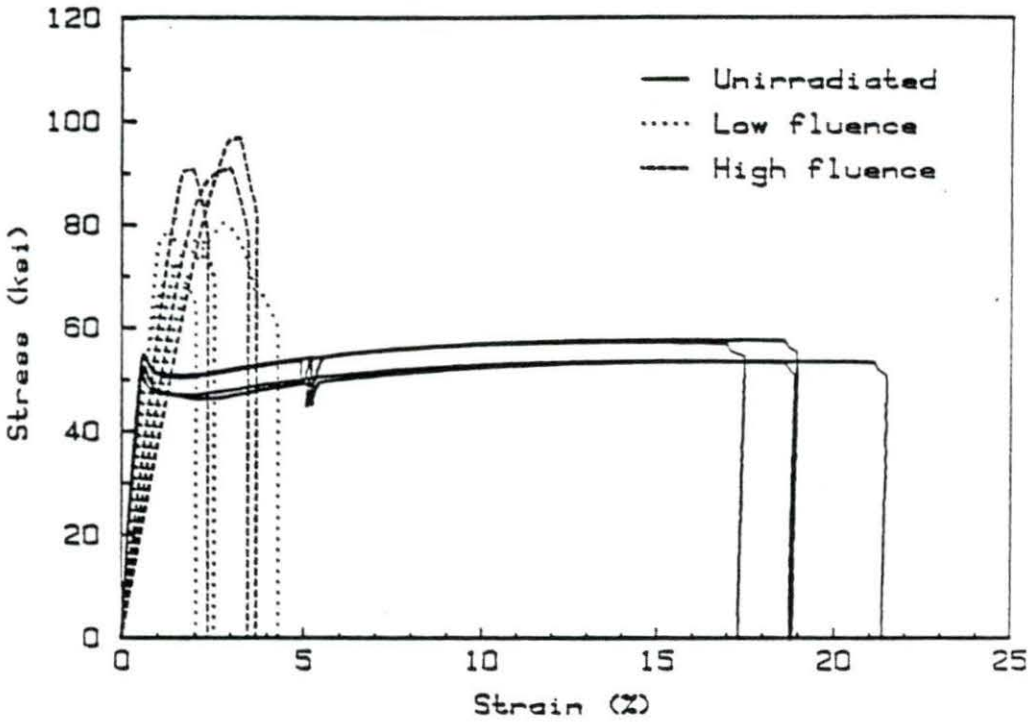

FIGURE 9. Experimental stress-strain curves for Ta

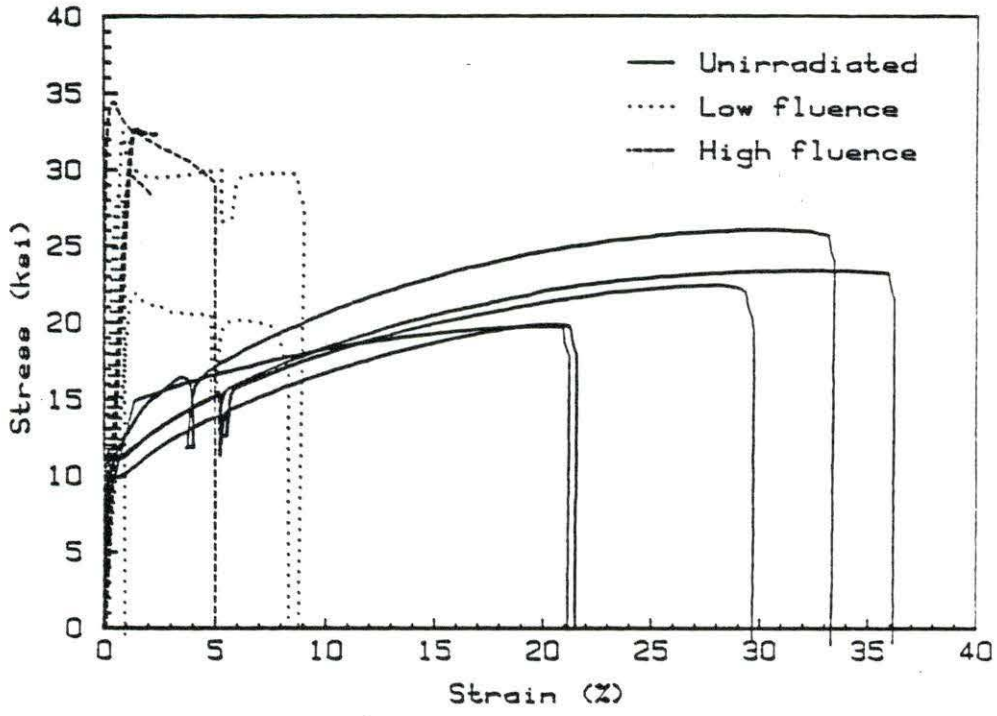

FIGURE 10. Experimental stress-strain curves for Fe

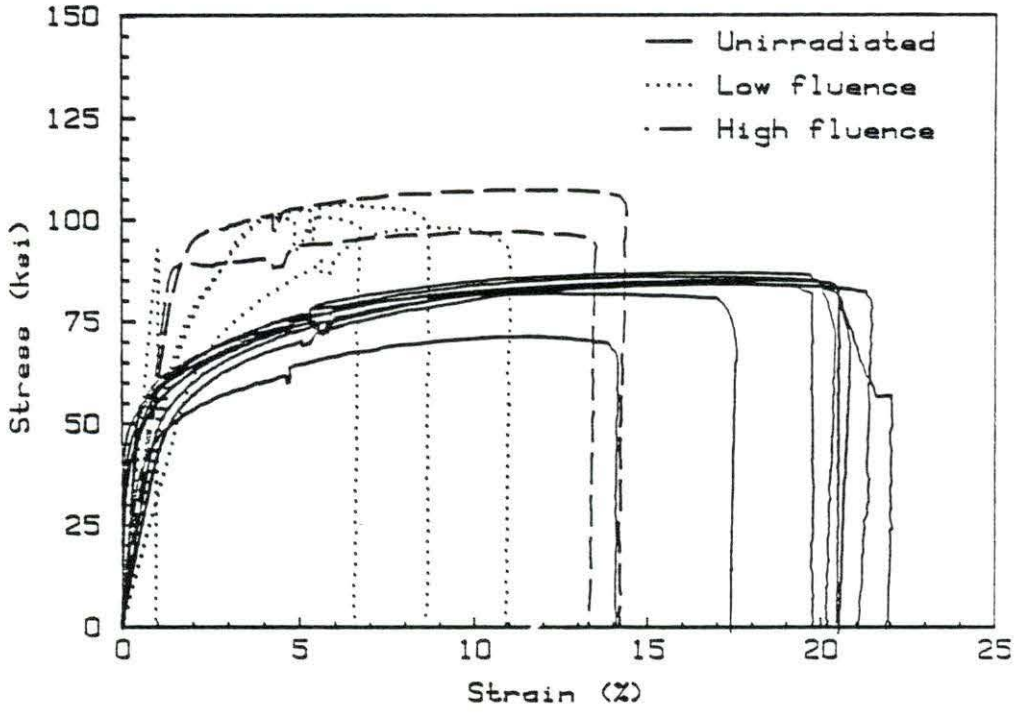

FIGURE 11. Experimental stress-strain curves for Fe-2.25Cr-1Mo

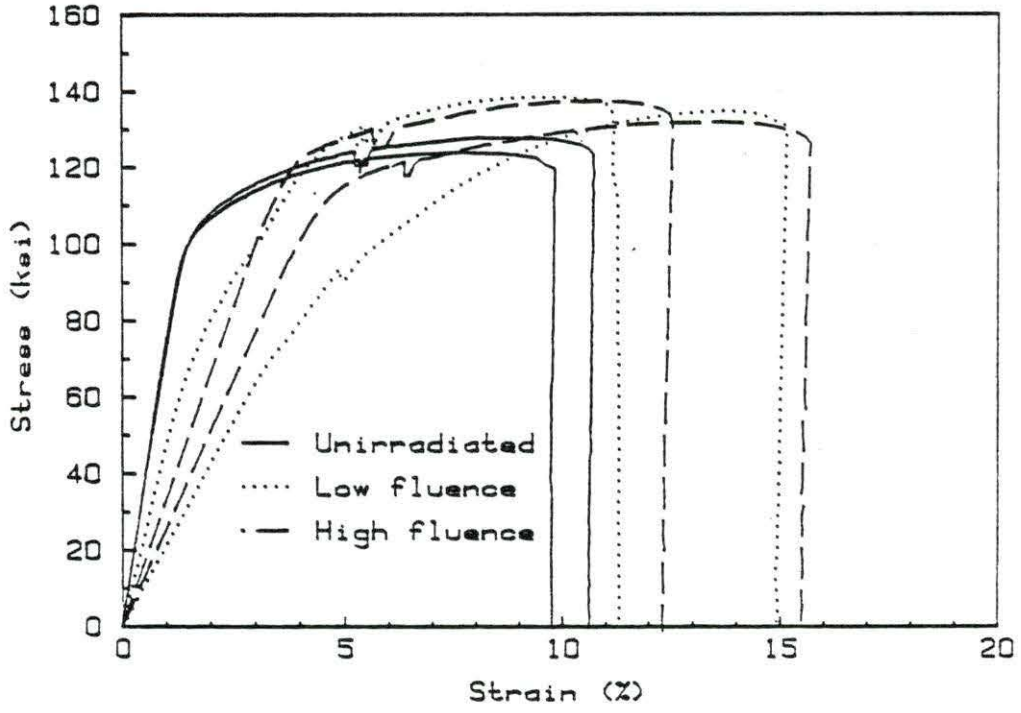

FIGURE 12. Experimental stress-strain curves for Fe-12Cr-1Mo

Tables 11-14 for all materials except Fe-12Cr-1Mo shows fairly good agreement. The values of n for the Fe-12Cr-1Mo alloy are about 45 percent higher than the true uniform strain.

Generally, the work hardening exponent decreased upon irradiation, and so did the uniform strain (Tables 11-14). The decrease in the work hardening exponent upon irradiation was also observed by other researchers [32,37]. This decrease is explained by the fact that once the elastic limit has been exceeded and deformation initiated, the deformation is confined to channels known as dislocation channels. After the passage of the first few slip dislocations, the radiation produced defects within the channels disappear and subsequent deformation occurs with less work hardening [37].

The application of the work hardening equation (4.2) yielded reasonably good fits to the experimental stress-strain curves. The stress-strain curves obtained, fitting data to the equation (4.2), are displayed in Figures 13-16 for Ta, Fe, Fe-2.25Cr-1Mo, and Fe-12Cr-1Mo, respectively. In Figure 17, the average curve for Ta is shown in the region between the lower yield stress and ultimate tensile strength. For each irradiation condition, the average values of K and n in Tables 11-14 were used in Figures 13-22.

In plotting the curves in Figures 13-16, it was assumed that the Young's modulus was unchanged upon irradiation, therefore, for all irradiation conditions, the elastic region was drawn having the slope of the unirradiated material.

In general, 800 MeV proton irradiation produced an increase in the yield stress and ultimate tensile stress and a decrease in the rate of work hardening and uniform strain. This was observed on pure metals Ta and Fe and iron base alloys Fe-2.25Cr-1Mo and Fe-12Cr-1Mo. Radiation-produced defects, such as point defects, impurity atoms, depleted zones, dislocation loops, cavities (voids and helium atoms), and precipitates, are responsible for strengthening and the loss of ductility. These defects serve as barriers to the motion of slip dislocations moving on slip planes. This increases the stress required to start a dislocation moving and to keep it moving.

The decrease in the rate of work hardening upon irradiation is associated with the microscopic phenomenon of the dislocation channeling. Dislocation channels have been observed in many metals and the mechanisms of dislocation channeling have been discussed by many researchers [38]. In this process, radiation-produced defects impeding dislocation motion in a metal are cleared away as the dislocation moves through them. Succeeding mobile

dislocations, therefore, face a smaller resistance to their motions. Thus, they move along the partially denuded glide plane more easily than the dislocations that first cleared the way. The stress required to move dislocations over slip planes that have been cleared of defects is much lower than the stress required to move first dislocations. Thus, an avalanche of dislocations is produced along the planar channels that have been cleared of defects. A group of parallel slip planes that have been cleared of obstacles by moving dislocations is called a dislocation channel and the process is called dislocation channeling [38]. As the number of channels increases, the material becomes softer. As a result of this, necking or plastic instability occurs more readily in irradiated materials.

A quick examination of Figures 13-16 shows that the yield stress and ultimate tensile strength increases and the work hardening and uniform strain decreases upon irradiation for the four materials. This increase in the yield stress and ultimate tensile strength is much larger for pure metals Ta and Fe than the two iron base alloys. However, these alloys show some work hardening following even high fluence irradiation, while pure metals exhibited plastic instability following plastic deformation.

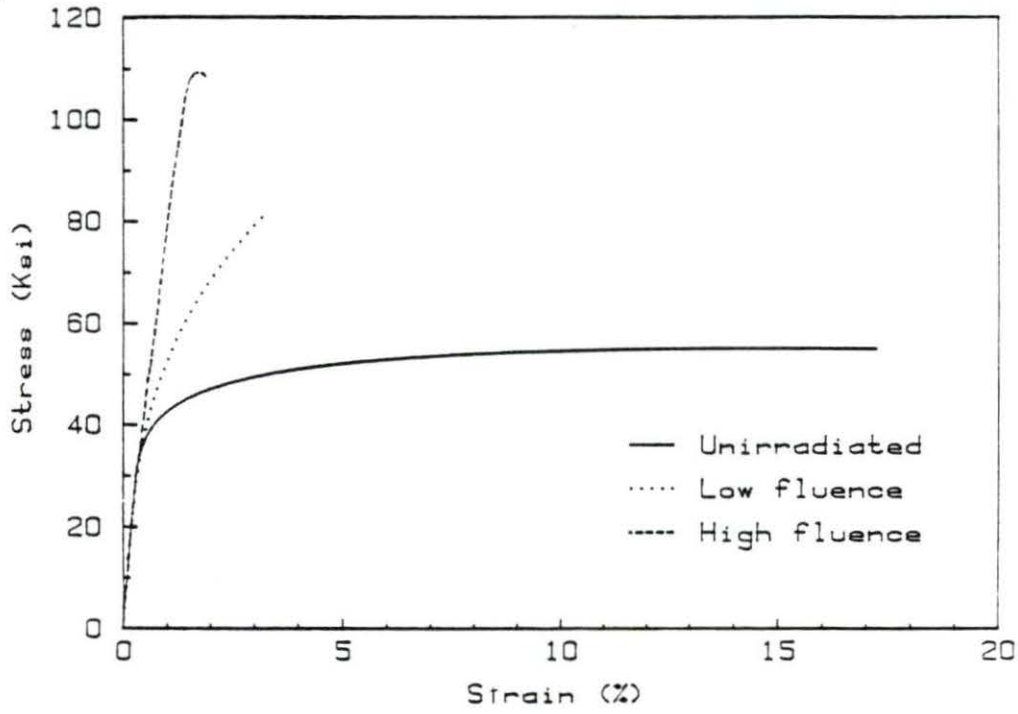

FIGURE 13. Effects of proton irradiation on tensile properties (stress-strain curves) of Ta

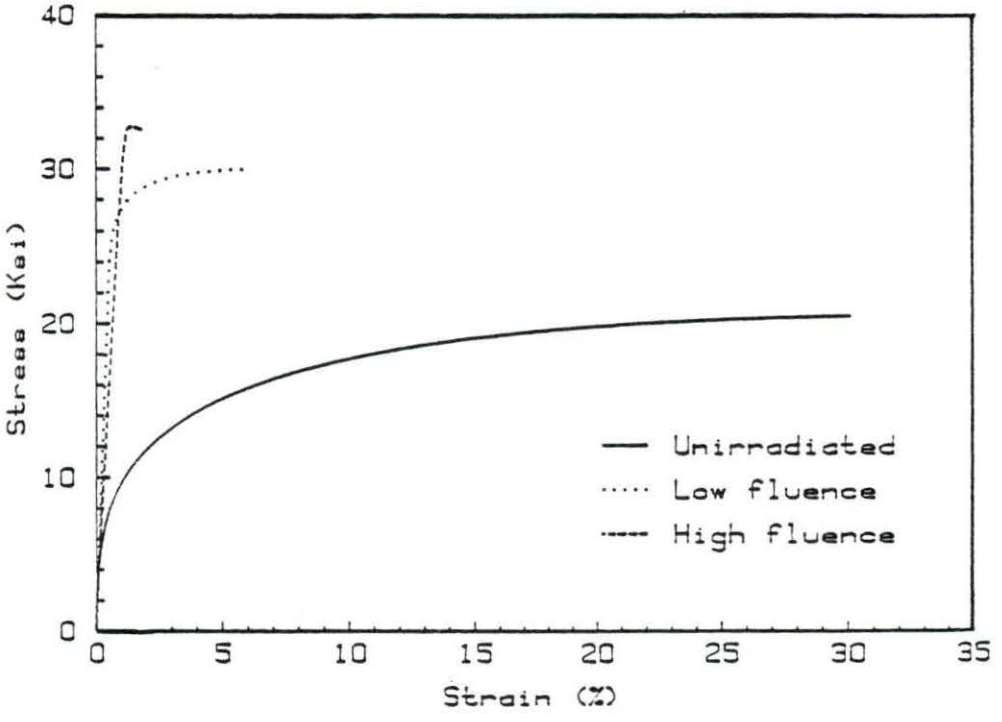

FIGURE 14. Effects of proton irradiation on tensile properties (stress-strain curves) of Fe

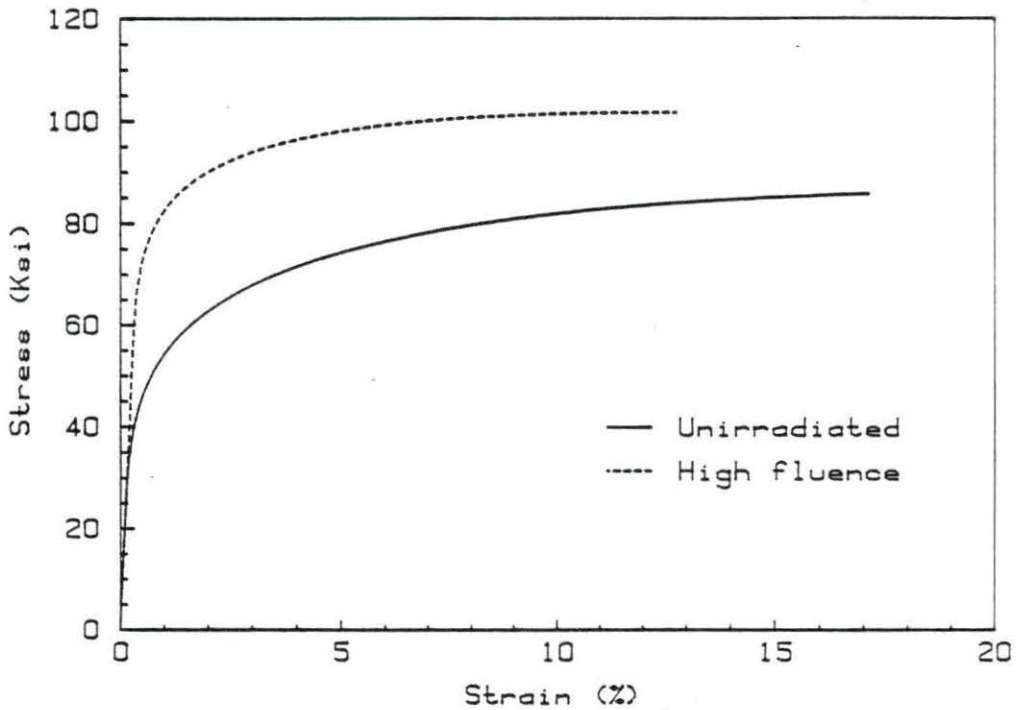

FIGURE 15. Effects of proton irradiation on tensile properties (stress-strain curves) of Fe-2.25Cr-1Mo

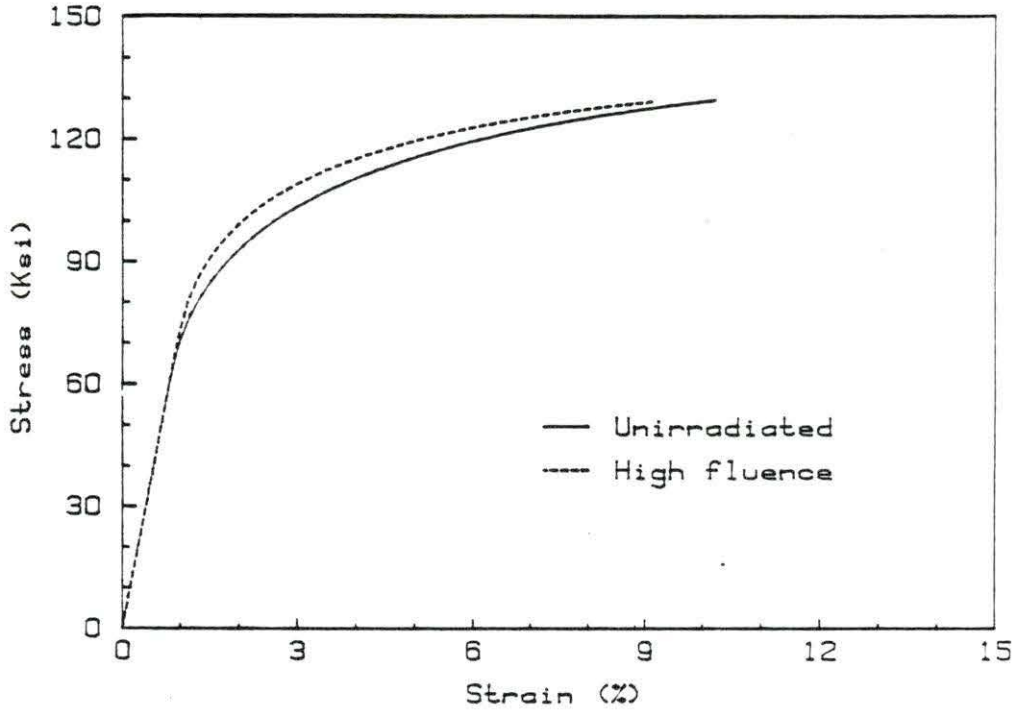

FIGURE 16. Effects of proton irradiation on tensile properties (stress-strain curves) of Fe-12Cr-1Mo

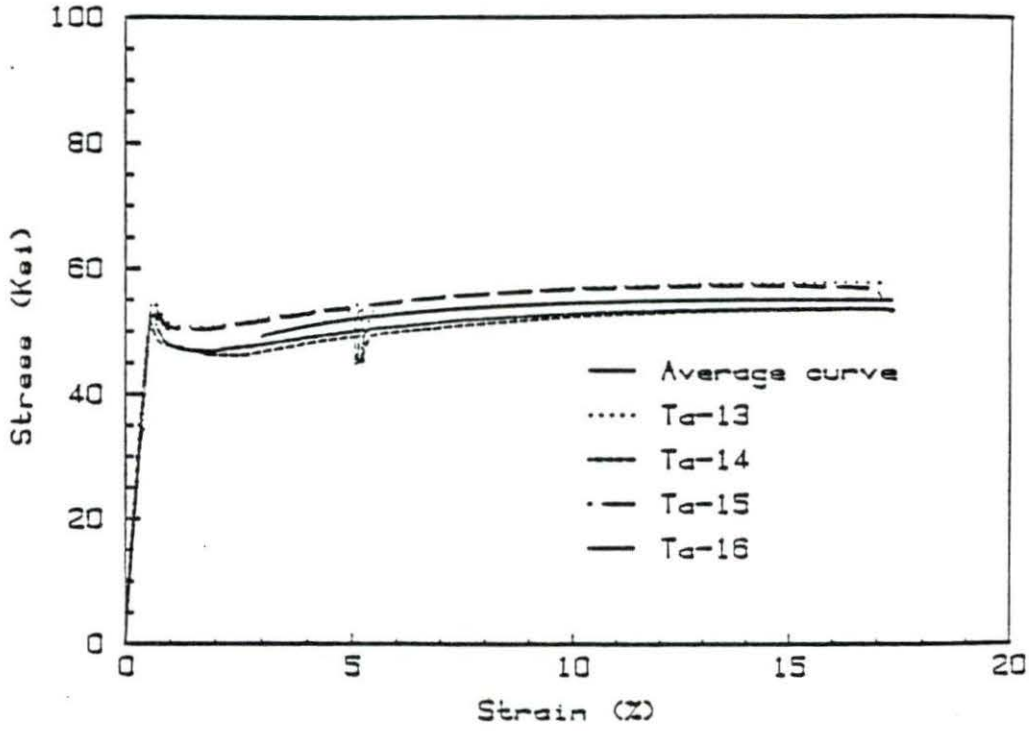

FIGURE 17. Average stress-strain curve obtained fitting data to $\bar{\sigma}=K\bar{\epsilon}^n$ and experimental stress-strain curves for unirradiated Ta samples

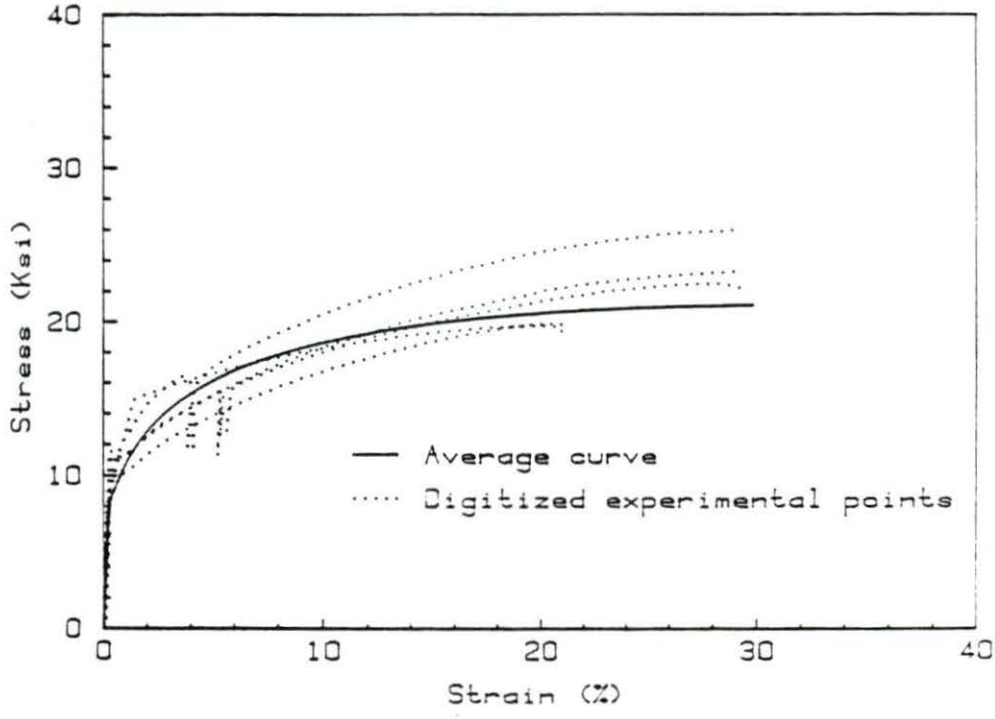

FIGURE 18. Average stress-strain curve obtained fitting data to $\bar{\sigma}=K\bar{\epsilon}^{n}$ and experimental stress-strain curves for unirradiated Fe samples

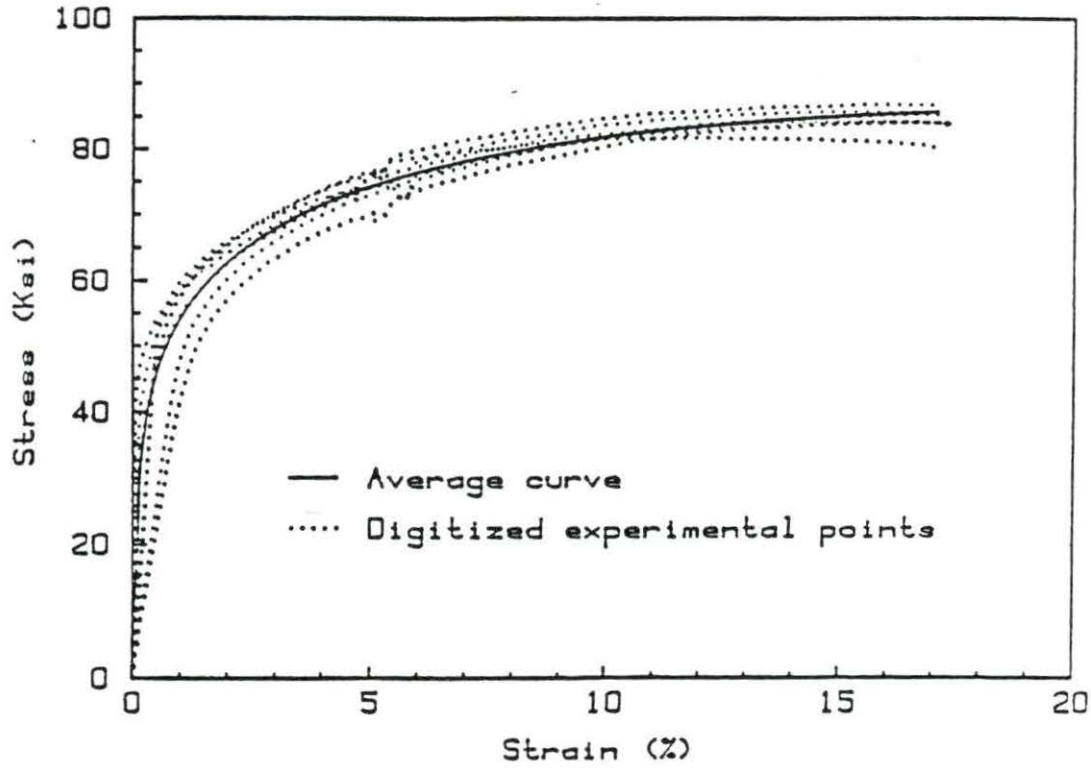

FIGURE 19. Average stress-strain curve obtained fitting data to $\bar{\sigma}=K\bar{\epsilon}^{n}$ and experimental stress-strain curves for unirradiated Fe-2.25Cr-1Mo samples

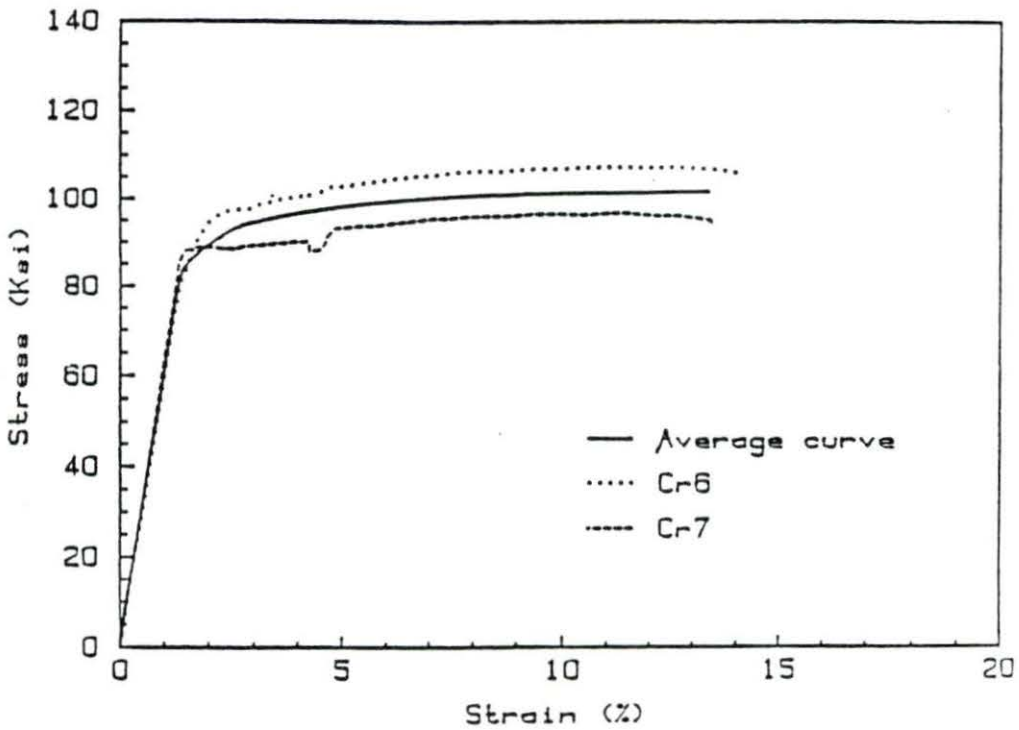

FIGURE 20. Average stress-strain curve obtained fitting data to $\bar{\sigma}=K\bar{\epsilon}^{n}$ and experimental stress-strain curves for high-irradiated Fe-2.25Cr-1Mo samples

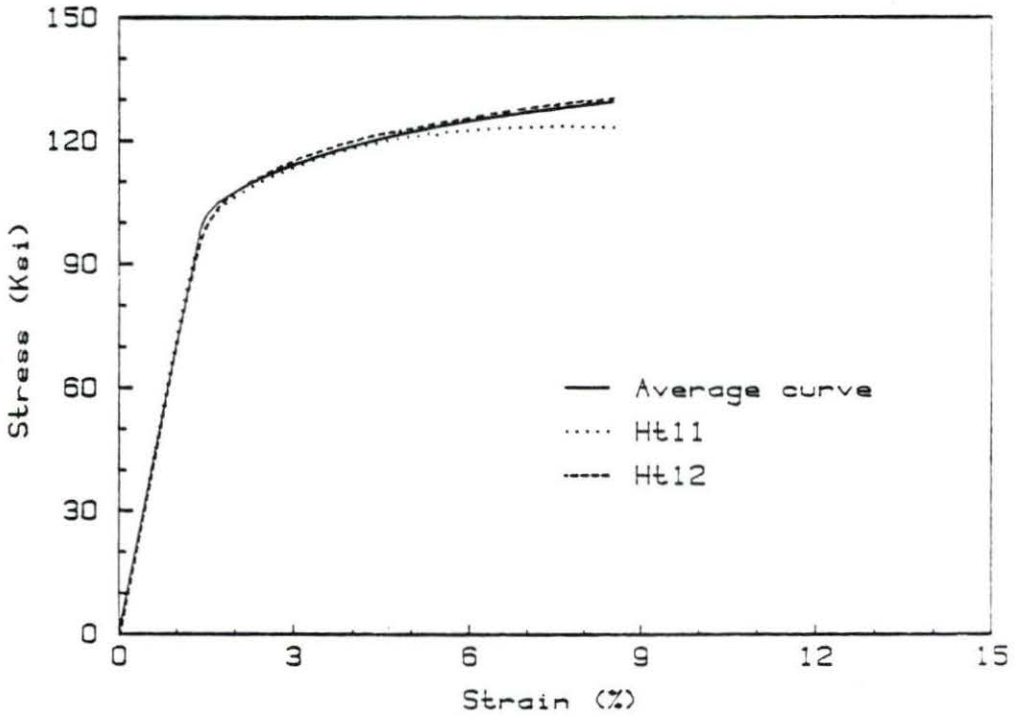

FIGURE 21. Average stress-strain curve obtained fitting data to $\bar{\sigma}=K\bar{\epsilon}^{n}$ and experimental stress-strain curves for unirradiated Fe-12Cr-1Mo (HT-9) samples

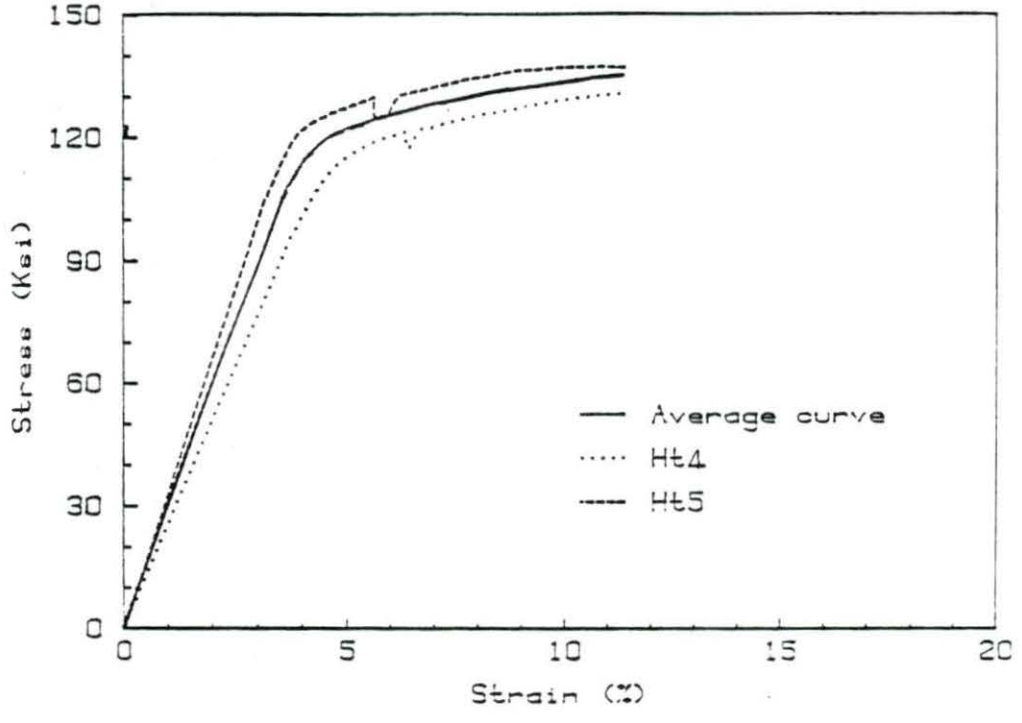

FIGURE 22. Average stress-strain curve obtained fitting data to $\bar{\sigma}=K\bar{\epsilon}^{n}$ and experimental stress-strain curves for high irradiated Fe-12Cr-1Mo (HT-9) samples

VI. SUMMARY AND CONCLUSION

In this work, the effects of 800 MeV proton irradiation on the stress-strain behavior were analyzed for Ta, Fe, Fe-2.25Cr-1Mo, and Fe-12Cr-1Mo (HT-9). The results can be summarized, as follows:

- It was not possible to draw conclusions concerning the effect of irradiation on Young's modulus.
- Reasonably good fits to the experimental stress-strain curves were obtained using the work hardening equation $\bar{\sigma}=K\bar{\epsilon}^{n}$.
- The work hardening exponent, n, decreased upon irradiation, and so did the uniform strain.
- Irradiation caused an increase in the yield strength and ultimate tensile strength and a decrease in ductility.
- The fractional increase in the yield strength and ultimate tensile strength and the fractional decrease in the work hardening and uniform strain is much larger for Fe and Ta than the iron base alloys Fe-2.25Cr-1Mo and Fe-12Cr-1Mo.

Since this work is completely based on the experimental stress-strain curves, the validity of the results presented in this work is largely dependent upon the accuracy of these curves. Thus, more studies and experiments need to be done to confirm the results of this work in order to have a

better understanding of the effects of 800 MeV proton irradiation on the tensile properties of the investigated four materials.

VII. REFERENCES

1. G. S. Bauer, Atomkernenergie Kerntechnik. 41, 234 (1982).

2. M. S. Wechsler and W. F. Sommer, J. Nuc. Mater. 122, 1078 (1984).

3. R. D. Brown, M. S. Wechsler, and C. Tschalaer, in Influence of Radiation on Material Properties, ASTM 956, edited by F. A. Garner et al. (American Society for Testing and Materials, Philadelphia, 1987), p. 1189.

4. R. L. Klueh and J. M. Vitek, J. Nuc. Mater. 126, 9 (1984).

5. N. Igata, K. Shibata, and S. Sato, Rad. Effects 41, 251 (1979).

6. D. Petroff and D. N. Seidman, Acta Met. 21, 323 (1973).

7. K. C. Wilson and D. N. Seidman, in Proc. Conf. on Defects and Defect Clusters in BCC Metals and Their Alloys, edited by R. J. Arsenault (NBS, Gaithersburg, 1973), p. 216.

8. D. N. Seidman, Cornell University Materials Science Center, Rep. No. 2564 (1975).

9. C. A. Coulter, D. M. Parkin, and W. V. Green, J. Nuc. Mater. 67, 140 (1977).

10. W. A. Coleman and T. W. Armstrong, Nuc. Sci. Eng. 43, 353 (1971).

11. H. W. Bertini, Phys. Rev. 188, 1711 (1969).

12. H. W. Bertini and M. P. Guthrie, Nuc. Phys. A169, 670 (1971).

13. D. M. Parkin and A. N. Goland, Rad. Effects 28, 31 (1976).

14. J. Lindhard, V. Nielsen, and M. Scharff, Mat. Fys. Medd. Dan. Vid. Selsk. 33, No. 10 (1968).

15. J. Lindhard, M. Scharff, and H. E. Schiott, Mat. Fys. Medd. Dan. Vid. Selsk. 33, No. 14 (1963).

16. J. Lindhard, V. Nielsen, M. Scharff, and P. V. Thomson, Mat. Fys. Medd. Dan. Vid. Selsk. 33, 10 (1963).

17. 1982 Book of ASTM Standards, E521-82, Part 45: Nuclear Standards (American Society for Testing and Materials, Philadelphia, 1982), p. 1132.

18. I. Manning and G. P. Mueller, Comp. Phys. Comm. 7, 85 (1974).

19. J. F. Janni, AWFL-TK-150, Air Force Weapons Laboratory, Kirtland Air Force Base, Albuquerque, New Mexico, 1966.

20. R. W. Conn, in Fusion, Volume 1, Magnetic Confinement, Part B (Academic Press, New York, 1981), p. 194.

21. W. F. Sommer, L. N. Kmetyk, W. V. Green, and R. Damjanovich, J. Nuc. Mater. 103 and 104, 1583 (1981).

22. W. F. Sommer, D. S. Phillips, W. V. Green, L. W. Hobbs, and C. A. Wert, J. Nuc. Mater. 114, 267 (1983).

23. J. Weertman and W. V. Green, J. Nuc. Mater. 75, 312 (1978).

24. W. F. Sommer, J. Weertman, W. V. Green, and L. N. Kmetyk, J. Nuc. Mater. 98, 190 (1981).

25. D. Farnum, W. Sommer, and O. Inal, J. Nuc. Mater. 122, 996 (1984).

26. W. V. Green, S. L. Green, B. N. Singh, and T. Leffers, J. Nuc. Mater. 104, 1221 (1981).

27. B. N. Singh, W. V. Green, T. Leffers, and S. L. Green, Scripta Met. 15, 1355 (1981).

28. B. N. Singh, T. Leffers, W. V. Green, and S. L. Green, J. Nuc. Mater. 105, 1 (1982).

29. W. F. Sommer, W. V. Green, L. W. Hobbs, C. A. Wert, and D. S. Phillips, J. Nuc. Mater. 114, 267 (1983).

30. H. Jang, J. Moteff, L. Levinson, R. D. Brown, and W. V. Green, J. Nuc. Mater. 98, 98 (1981).

31. S. L. Green, J. Nuc. Mater. 126, 30 (1984).

32. R. Brown and J. Cost, in Effects of Radiation on Materials:Eleventh International Symposium, ASTM STP 782, edited by H. R. Brager and J. S. Perrin (American Society for Testing and Materials, Philadelphia, 1982), p. 917.

33. J. Cost and W. Sommer, J. Nuc. Mater. 103, 773 (1981).

34. C. R. Barrett, W. D. Nix, and A. S. Tetelman, The Principles of Engineering Materials (Prentice-Hall Inc., Englewood Cliffs, New Jersey, 1973), p. 234.

35. J. Marin, The Mechanical Behavior of Engineering Materials (Prentice-Hall Inc., Englewood Cliffs, New Jersey, 1962), p. 31.

36. J. Neter and W. Wasserman, Applied Linear Statistical Models (Richard-Irwin Inc., Illinois, 1974), p. 89.

37. E. E. Bloom and J. R. Weir, Nucl. Technol. 16, 45 (1972).

38. M. S. Wechsler, in The Inhomogeneity of Plastic Deformation, edited by R. E. Hill (American Society for Metals, Metals Park, Ohio, 1973), p. 19.

39. Metals Handbook. Ninth Edition, Volume 1. Properties and Selection: Iron and Steels (American Society for Metals, Metals Park, Ohio, 1978).

VIII. ACKNOWLEDGMENTS

The author wishes to express sincere appreciation and thanks to his major professor, Dr. Monroe S. Wechsler, for his invaluable guidance, advice, and prompt assistance and support during the course of this study.

Thanks are also due to Dr. Robert D. Brown of the Los Alamos National Laboratory for his kindness in making available the original experimental tensile test results that were analyzed in this work. Appreciation is also extended to Dr. David M. Martin of the Department of Materials Science and Engineering at Iowa State for his kind consideration in providing information and facilities required for much of the computational work. Sincere thanks go also to Zekeriya Altac, Uner Colak, Niyazi Sokmen, Feyzi Inanc, and Okan Zabunoglu for their friendship and for the help they provided through many valuable discussions.

In addition, the author wishes to express sincere appreciation to his government, the Republic of Turkey, for its financial support during his study.

Finally, he wishes to give a special acknowledgment with deep appreciation to his parents, brother and sisters, whose love, faith, understanding, and encouragement were essential ingredients during his studies in America.